

**OMAE2011-50283**

## **NUMERICAL WAVE TANK ANALYSIS OF WAVE RUN-UP ON A TRUNCATED VERTICAL CYLINDER**

Jang Kim  
Technip

Rajeev Jaiman  
ACUSIM Software, Inc.

Steve Cosgrove  
ACUSIM Software, Inc.

Jim O'Sullivan  
Technip

### **ABSTRACT**

A new far-field closure condition for a CFD-based numerical wave tank that uses a potential wave solution to overlay the outer computational domain of a CFD solution is described. A prescribed potential wave solution covers the region beyond a diameter more than 10 times of floater footprints. The diffracted waves from the body are absorbed by the 'potential-attractor' terms applied in the intermediate CFD domain where the CFD solution for Navier-Stokes equation is gradually blended into far-field potential solution. The proposed model provides an efficient numerical wave tank for the case when incoming wave length is much longer than floater. In this case, the required mesh and domain size for numerical accuracy is mainly affected by the floater geometry and local wave kinematics near the floater and less dependent on the length scale of the incoming waves. The new numerical wave tank is first tested for a diffraction of a truncated cylinder exposed to long regular waves. Comparison with theoretical and experimental results demonstrates accuracy and efficiency of the new method.

### **INTRODUCTION**

A new hybrid numerical method matches a potential solution at far field with a CFD solution near the structure. In the proposed method, a potential wave solution overlays the outer computational domain of CFD solution, which usually covers diameter less than 10 times of floater footprints. The diffracted waves from the body are absorbed by the momentum and mass source terms applied in the intermediate CFD domain where a viscous-flow solution at near field is gradually blended into the far-field potential solution.

The proposed numerical method requires smaller computational domain than the physical wave tank because

wave maker and fluid domain near the wave maker do not need to be modeled. The computational domain can be further confined near the floater depending on the required size of intermediate zone where the diffracted waves are absorbed. Previous experience from potential-based numerical wave tank using similar far-field closure condition shows that the required computational domain can be confined near the body when incoming wave length is much longer than the free-surface footprint of the floater [1, 2]. This is due to the fact that diffracted waves are mostly higher-order waves with wave length comparable to the floater dimensions.

The proposed method will provide an efficient CFD tool for air-gap analysis of a floating structure under harsh environment such as Gulf of Mexico and North Sea. Environments in these areas can be characterized by large wave heights and long wave lengths. The design wave condition for air-gap analysis usually provides wave length more than 10 times longer than free-surface foot prints of floaters. Under these circumstances, the diffracted wave based on linear wave theory is negligibly small. However, experimental results shows wave elevation due to diffraction can be as high as two times of the wave amplitude in case of wave run-up on sing-column floater [3, 4]. In case of multi-column floaters, the interaction between diffracted waves from multiple columns and incident wave can generate maximum wave elevation as high as three times of the wave amplitude [5]. Applying the second-order theory improves accuracy of theoretical prediction for moderate wave steepness. However, for the extreme design waves, the second-order theory still under predicts the maximum wave elevation of the diffracted wave [3,4].

CFD tools that can consider free-surface nonlinearity and detail body geometry are presenting promising results for free-surface problems[6]. However, because of the large length-scale difference between wave and floating body, CFD

simulation must deal with proper details of body geometry, near-field wave interaction and a computational domain large enough to prevent wave reflection. This demands significant computational resources. Furthermore, in case of CFD codes based on Navier-Stokes solver, computational domain away from the floaters also requires fine mesh near the free-surface to prevent excessive attenuation of incident wave due to numerical damping; this increases the computational requirements.

The above factors make the proposed method more attractive for the air gap analysis of floating structures under the extremely long and high incoming waves. In the proposed method, a potential wave solution overlays the outer computational domain of CFD solution, which usually covers diameter less than 10 times of floater footprints. The diffracted waves from the body are mostly second- and third-order waves with wavelengths four- and nine times shorter than the incoming wave. These waves can be effectively absorbed with small size of intermediate CFD domain where the diffracted waves are absorbed by mass and momentum source distributed in the fluid domain.

In this paper, implementation of the proposed method uses the commercial CFD code AcuSolve, which is based on the Galerkin/Least-Squares formulation and uses Arbitrary Lagrangian Eulerian (ALE) to simulate free-surface effects. The far-field potential solver and source terms to be added to the near-field solver uses a library of user-defined function customized to AcuSolve.

The numerical wave tank model is applied to a two-dimensional wave flume simulation to demonstrate validity of far-field closure condition. Then the model is applied to the diffraction of long nonlinear Stokes wave by a truncated vertical cylinder, which is a simplified form of a single-column floater. Two geometries of numerical wave tank, rectangular and circular tank, are tested. Calculated wave run up is compared with first- and second-order potential theory and experimental data. The numerical results show that the new numerical wave tank model provides accurate wave run up with a small computational domain.

## METHOD OF SOLUTION

A free-surface flow of an incompressible fluid in the water of constant depth,  $h$ , is considered. A Cartesian coordinate system  $Oxyz$ , where the  $z$ -axis directs against gravity and the  $Oxy$ -plane is the still water level is used as shown in Fig. 1. The location of the free surface is denoted by  $z = \zeta(x, y, t)$  and the bottom as  $z = -h$ . The fluid domain is denoted by  $D$ , and the boundaries of the fluid domain on the free surface, sea bottom and floater are denoted by  $S_F$ ,  $S_B$  and  $S_0$ , respectively. The lateral boundary of the fluid domain extends to far infinity.

At the far field, we assume that the fluid motion is irrotational such that we introduce velocity potential  $\phi(x, y, z, t)$  to describe the fluid motion. The velocity potential

is governed by the Laplace equation in the fluid domain with appropriate conditions on the boundaries.

In the near field around floater, the Navier-Stokes equations are solved by an Arbitrary-Lagrangian-Eulerian (ALE) formulation [7]. The ALE formulation allows an accurate treatment of material surfaces, i.e., free-surface particle motions. The free-surface physical conditions required on a material surface are: (a) no particles cross it, and (b) tractions must remain continuous across the surface.

The moving ALE mesh solution algorithm has three steps: (i) Solve Navier-Stokes equation for velocity and pressure; (ii) Update the free-surface conditions; and (iii) Adapt the interior mesh and compute ALE mesh velocities. A hyperelastic model problem is solved for unknown fluid mesh nodal displacements and velocities.

The near-field Navier-Stokes solution is matched to the potential solution at the intermediate-field, where ‘‘potential attractor’’ terms are added to the Navier-Stokes equations. The governing equations and boundary conditions in those three subdomains are described as follows:

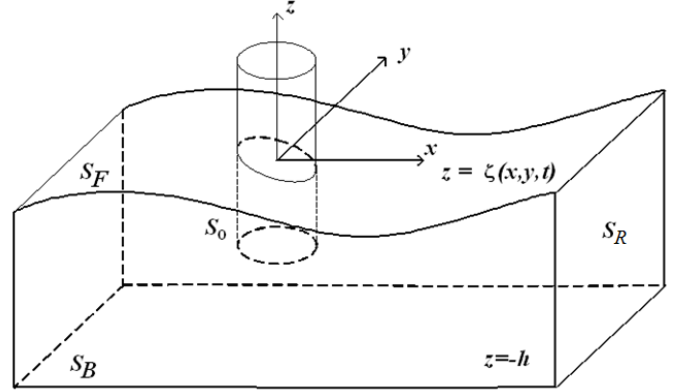


Figure 1 Definition sketches of the computational domain

## Navier-Stokes Problem at Near Field

The transient Navier-Stokes equation in the ALE coordinates are given by

$$\begin{aligned} \rho u_{i,t} + \rho(u_j - \hat{u}_j)u_{i,j} + p_{,i} - \tau_{ij,j} - \rho b_i &= 0 \text{ in } D \\ \rho_{,t} + (\rho u_i - \rho \hat{u}_i)_{,i} &= 0 \text{ in } D \\ \tau_{ij} &= \mu_{eff}(u_{i,j} + u_{j,i}) \end{aligned} \quad (1)$$

where  $\rho$  is the density (which is assumed to be constant throughout);  $\mathbf{u}$  denotes the fluid velocity vector;  $\hat{\mathbf{u}}$  denotes the fluid mesh velocity vector;  $p$  is the pressure;  $\boldsymbol{\tau} = [\tau_{ij}]$  is the viscous stress tensor;  $\mathbf{b}$  is the specific body force;  $\mu_{eff}$  denotes effective viscosity that accounts for both molecular and turbulent eddy viscosities. The following sets of Dirichlet and Neumann boundary conditions are imposed as:

$$\begin{aligned}
u_i &= 0 \quad \text{on } S_o, S_B \\
\hat{u}_j n_j &= u_j n_j + q \quad \text{on } S_F \\
P_f &= (-pn_i + \tau_{ij} n_j) = 0 \quad \text{on } S_F
\end{aligned} \tag{2}$$

where  $q$  and  $P_f$  are mass flux and traction on the free surface. The specific body force  $\mathbf{b}$  and mass flux  $q$  are zero in the near field. Non-zero values of body force and mass flux will be applied in the intermediate field, which will be described later. In particular, on the free surface, we need to satisfy the kinematic boundary condition

$$\hat{\mathbf{u}} \cdot \mathbf{n} = \mathbf{u} \cdot \mathbf{n} \quad \text{on } S_F$$

where  $\hat{\mathbf{u}}$  denotes ALE velocity,  $\mathbf{n}$  is the outward unit normal to the fluid domain. This is the only way Navier-Stokes equations affects the ALE equation. The unknown positions of free surfaces are computed by simply imposing the obvious condition that no particle can cross the free surface (because it is a material surface). The mesh position, normal to free surface, is determined from the normal component of the particle velocity and the mesh motion is achieved by solving hyperelastic model for fluid mesh [7]. In summary, the above conditions correspond to the kinematic condition; and the dynamic condition expresses the traction-free situation. The traction-free condition:

$$\mathbf{P}_f = (-pn_i + \tau_{ij} n_j) = \mathbf{0}$$

is homogenous natural boundary condition and it is directly taken into account by the weak formulation of Navier-Stokes equations with stabilized finite element formulation.

The near field solutions shown herein are produced using the AcuSolve™ finite element Navier-Stokes solver based on the Galerkin/Least-Squares (GLS) formulation [9]. The GLS formulation provides second order accuracy for spatial discretization of all variables and utilizes tightly controlled numerical diffusion operators to obtain stability and maintain accuracy. In addition to satisfying conservation laws globally, the formulation implemented in *AcuSolve* ensures local conservation for individual elements. Equal-order nodal interpolation is used for all working variables, including pressure and turbulence equations. The semi-discrete generalized-alpha method is used to integrate the equations in time for transient simulations. The resultant system of equations is solved as a fully coupled pressure/velocity matrix system using a preconditioned iterative linear solver. The iterative solver yields robustness and rapid convergence on large unstructured industrial meshes even when high aspect ratio and badly distorted elements are present. With regard to the ALE free-surface formulation, the underlying Navier-Stokes system (1) is constructed such a way that it satisfies local and global conservation of mass and momentum for moving meshes.

### **Potential Problem at Far Field**

The governing equation in the fluid domain is given by

$$\nabla^2 \phi = 0 \quad \text{in } D \tag{3}$$

The bottom of the fluid domain is assumed to be flat and constant depth of  $h$ . The normal velocity of the fluid vanishes on the sea bottom:

$$\frac{\partial \phi}{\partial z} = 0 \quad \text{on } z = -h \tag{4}$$

On the free surface,  $S_f$ , the kinematic and dynamic conditions can be written as:

$$\frac{\partial \zeta^*}{\partial t} = \frac{\partial \phi}{\partial z} - \frac{\partial \phi}{\partial x} \frac{\partial \zeta^*}{\partial x} - \frac{\partial \phi}{\partial y} \frac{\partial \zeta^*}{\partial y} \quad \text{on } S_F \tag{5}$$

$$\frac{\partial \phi}{\partial t} + \frac{1}{2} \nabla \phi \cdot \nabla \phi + g \zeta^* = 0 \quad \text{on } S_F \tag{6}$$

where  $\mathbf{g}$  is gravity. The far-field potential solution is obtained in an infinite domain with uniform depth without floaters.

### **Matching at Intermediate Field**

Since we cannot solve infinite fluid domain, the radiation condition at the far infinity is replaced by numerical matching conditions at the finite truncated boundary  $S_R$ :

$$\mathbf{u} = \nabla \phi \quad \text{on } S_R \tag{7}$$

Also applied are “potential-attractor” terms, specific body force inside fluid domain and mass flux on the free-surface, which force the CFD solution to be matched with the potential solution:

$$q = -\mu(x, y)(\zeta - \zeta^*) \quad \text{on } S_F \tag{8}$$

$$b_i = -\mu(x, y)(u_i - \phi_{,i}) \quad \text{in } D \tag{9}$$

The damping function  $\mu(x, y)$  changes from zero at the inner area of  $S_f$  to a constant value at the outer area of  $S_f$ . More specific shape of the damping function will be provided later in the numerical examples. Similar approach has been successfully applied to match three-dimensional potential solution in the near field with the far-field two-dimensional potential solution [2].

### **FAR-FIELD INCOMING WAVE**

The far-field wave solution  $\zeta^*$  can be any nonlinear transient wave solution. In this study, we restricted the solution to the Stokes waves, or the nonlinear progressive waves with permanent form. The same finite-element method and the

Newton's method that were used for the solitary wave solution by Bai & Kim [8] has been used here for the numerical solution of Stokes waves. Vertical velocity-potential profile is approximated by Chebychev polynomial and piecewise-linear finite-element has been used for the horizontal interpolation.

Figure 2 and 3 show the convergence of a Stokes wave solution used in the numerical wave tank simulation.  $N_p$  denotes the number of Chebychev polynomials used in the vertical interpolation. Free-surface elevation and velocity profile at wave crest calculated with three different number of vertical interpolation,  $N_p$ , are compared. Numerical solution with  $N_p = 5$  shows quite converged solution. The maximum difference between  $N_p = 5$  and  $N_p = 7$  is less than 0.0005 % in wave elevation and 0.1 % in the velocity profile. In the numerical wave tank simulation presented in this paper, numerical solution with  $N_p = 7$  is used. In horizontal direction, total 800 mesh is used in one wave length, which provides sufficient accuracy for the waves considered.

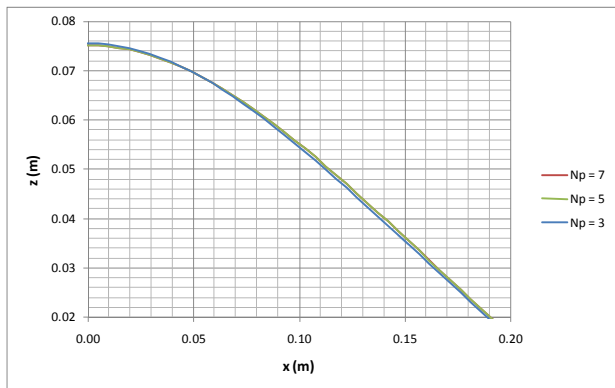


Fig. 2 Convergence of Potential Solution – Wave Elevation near Crest (  $h = 1\text{m}$ ,  $T = 0.98\text{ s}$ ,  $kA = 0.244$  )

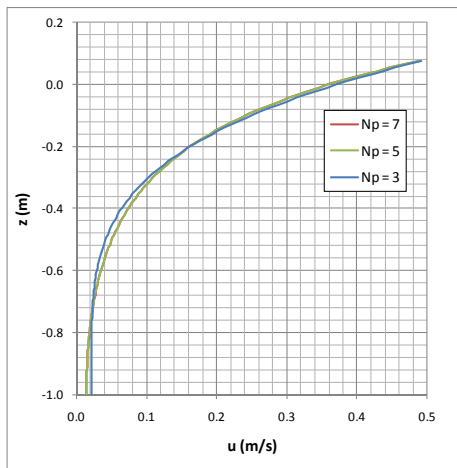


Fig. 3 Convergence of Potential Solution - Velocity Profile (  $h = 1\text{m}$ ,  $T = 0.98\text{ s}$ ,  $kA = 0.244$  )

## TWO-DIMENSIONAL WAVE-FLUME TEST

The validity of the proposed matching scheme is first tested by two-dimensional wave-flume simulation. The following parameters are used for the wave-flume test:

CFD Domain:  $L = 6.7\text{ m}$ ,  $h = 1\text{ m}$   
 Input Wave:  $T = 0.98\text{ s}$ ,  $\lambda = 1.5\text{ m}$ ,  $kA = 0.244$

where  $L$  and  $\lambda$  denote the length of wave flume and wavelength, respectively. The computational domain contains about 4.5 waves. The finite-element mesh system used for the simulation is shown in Fig. 4. Near the free-surface, finer meshes with 0.01 m length are used. Coarser mesh has been used near the tank bottom.

The intermediate-field domain of 0.5 m lengths are placed at the two ends of computational domain. The damping function,  $\mu(x)$ , is shown in Fig. 5(a). Fig. 5(b) & (c) compare instantaneous wave and horizontal velocity at  $t = 0$  and  $t = 6.9\text{ s}$ . Waves are propagating from left to right. The initial condition at  $t = 0$  is identical to the input potential solution. Surface elevation and velocity contour from initial potential solution and CFD solution at  $t = 6.9\text{ s}$  compare quite well each other with minor local disturbances near the truncation boundaries. Fig. 5(d) compares the computed crest and trough height with the input Stokes waves. Oscillation in the crest height can be used to measure reflection and attenuation of numerical wave. In the present test results, crest height oscillation is less than 3% of the incoming wave crest height. This is less than typical wave reflection coefficient in physical wave tanks, which is generally higher than 5%. Harmonic components of the wave elevations are calculated from the last two periods of simulation and compared with the harmonic components of incoming wave in Fig. 5(e). The mean and second-harmonic components are nondimensionalized by  $kA^2$ , first harmonic components by  $A$ , and the third harmonic components by  $k^2A^3$ , where  $k$  and  $A$  are defined as wave number and first harmonic component, respectively. All harmonic components from CFD solution agrees well with the input wave components. Largest deviation occurs in the second-order mean component, which contributes increase of mean surface elevation about 2% of the first harmonic component.

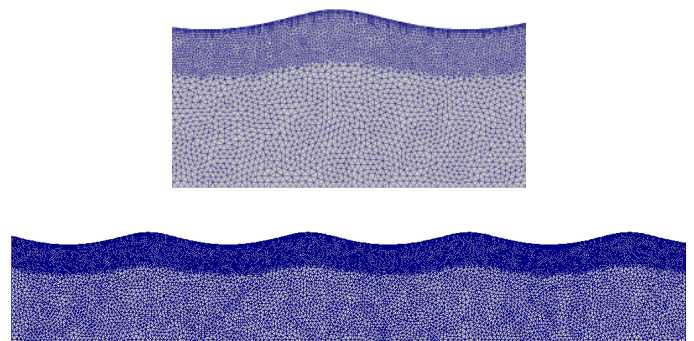
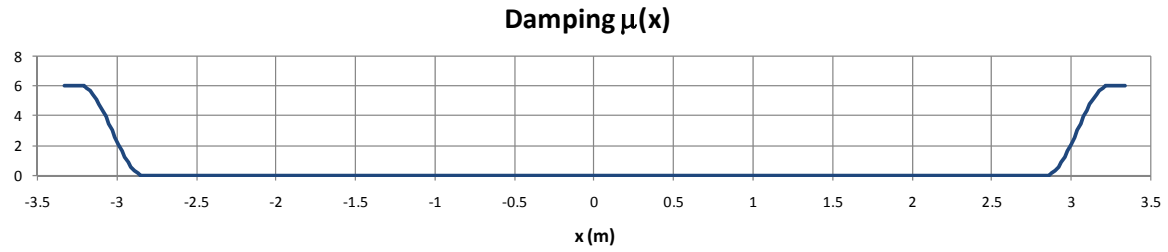
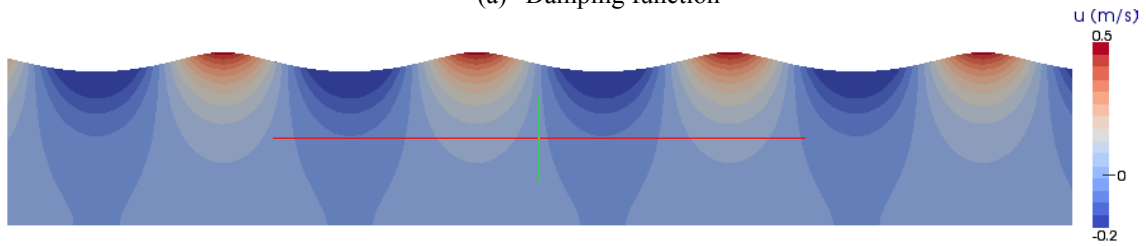


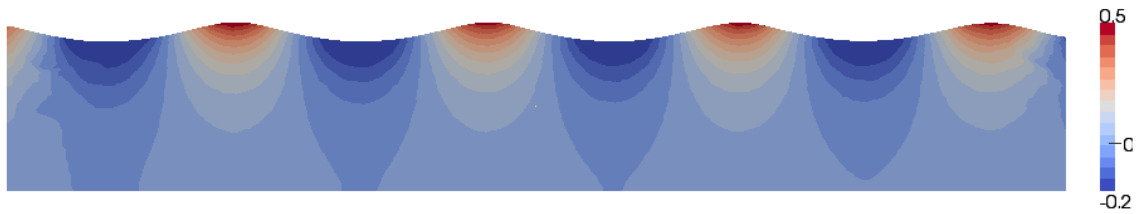
Fig. 4 Finite-Element Mesh for Two-Dimensional Wave-Flume Simulation



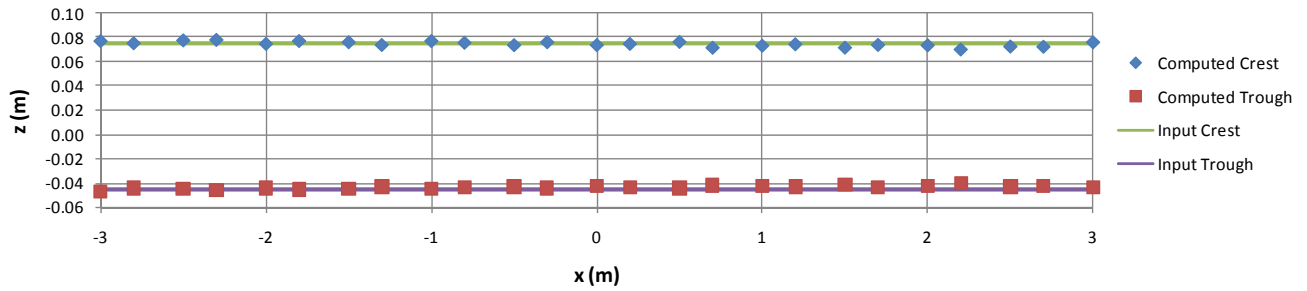
(a) Damping function



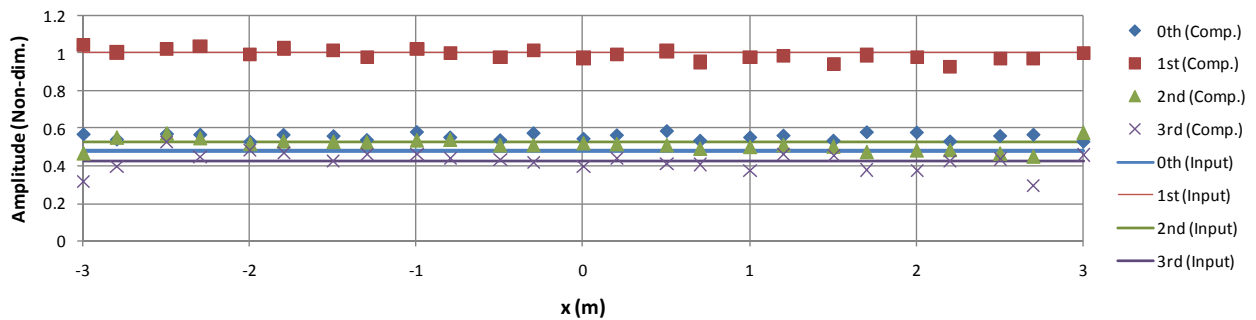
(b) Initial wave elevation and horizontal-velocity contour at  $t = 0.0$  s



(c) Wave elevation and horizontal-velocity contour at  $t = 6.9$  s



(d) Wave crest and trough height at wave gauges



(e) Harmonic components of wave elevation at wave gauges

Fig. 5 Two-dimensional Wave-Flume Simulation Results ( $h = 1\text{ m}$ ,  $T = 0.98\text{ s}$ ,  $kA = 0.244$ )

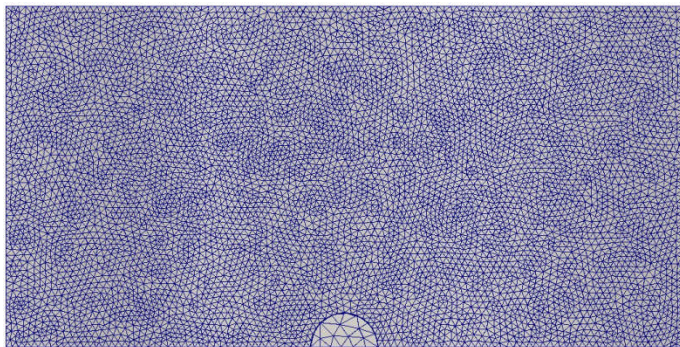
### DIFFRACTION BY A TRUNCATED CYLINDER

The run-up of Stokes wave on a truncated circular cylinder, with radius  $a = 0.15$  m and draft  $d = 0.87$  m, has been simulated. Two wave system with the following parameters are simulated:

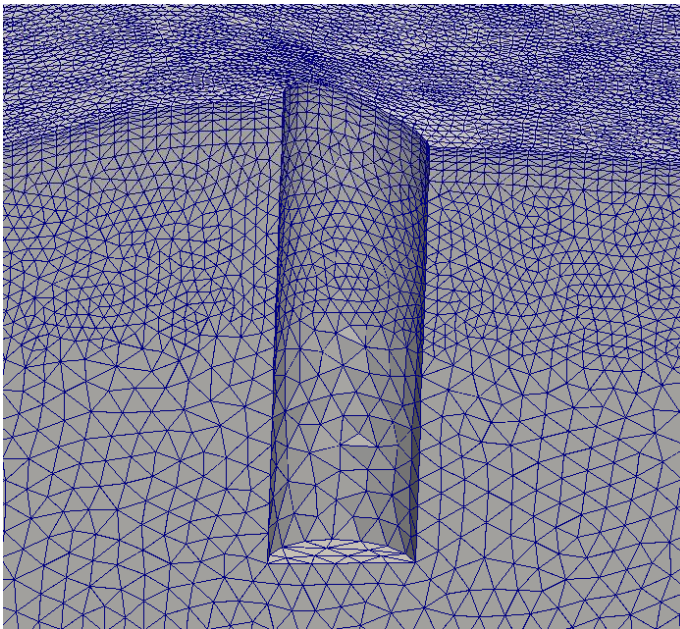
Case 1:  $T = 1.2$  s,  $\lambda = 2.25$  m,  $kA = 0.244$

Case 2:  $T = 1.7$  s,  $\lambda = 4.5$  m,  $kA = 0.16, 0.20, 0.22, 0.23$

The Case 1 wave is the same wave system that was tested in the two-dimensional wave-flume simulation. Case 2 waves are with wave length two times longer than Case 1. Three different wave steepness are tested. The simulated results are compared with the model test data and the second-order WAMIT results from [4].

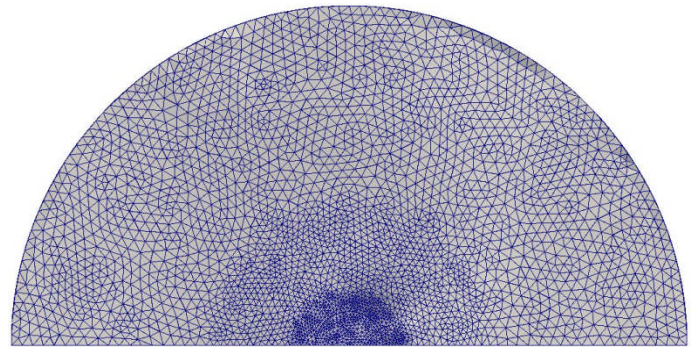


(a) Plan View

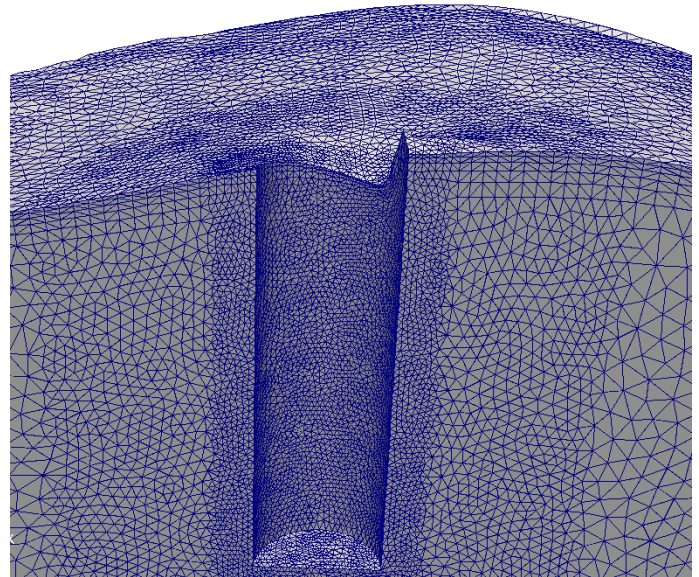


(b) Side View

Fig. 6 Finite-Element Mesh for a Rectangular Numerical Wave Tank



(a) Plan View



(b) Side View

Fig. 7 Finite-Element Mesh for a Circular Numerical Wave Tank

Rectangular domain with the size

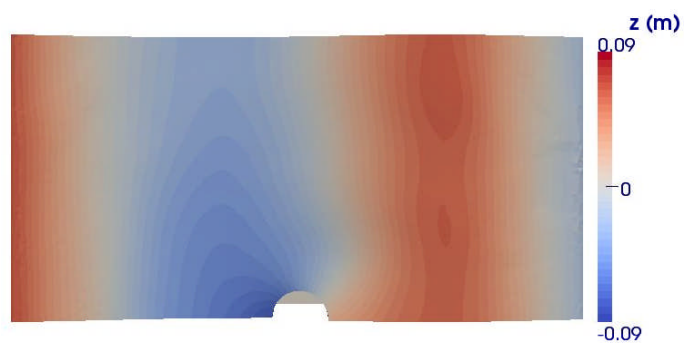
$$L \times B \times h = 3 \text{ m} \times 1.5 \text{ m} \times 1.5 \text{ m}$$

has been used for the Case 1. For Case 2 wave, circular domain with

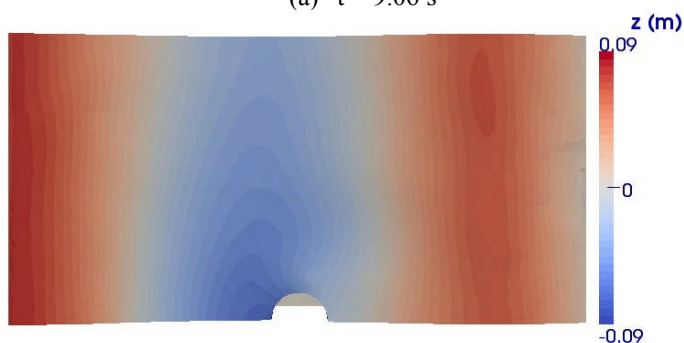
$$\text{Radius} = 1.5 \text{ m}, \quad h = 1.5 \text{ m}$$

has been used. The radius of circular domain is one third of the incoming wave length. Fig 6 and 7 show the finite-element mesh for the two cases, respectively.

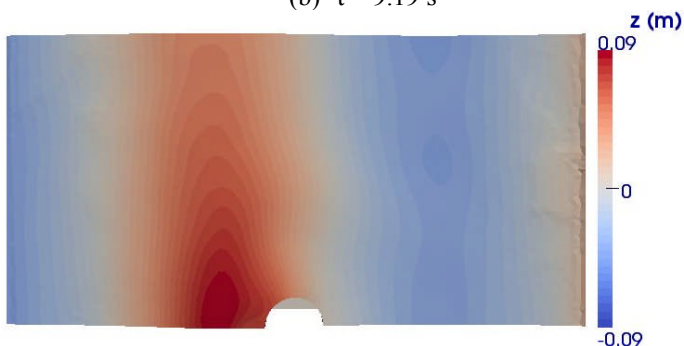
Fig. 8 shows the contour plots of free-surface elevation for Case 1 at three different time steps. It can be seen that wave enters and exits the computational domain with little reflection from the outer boundary.



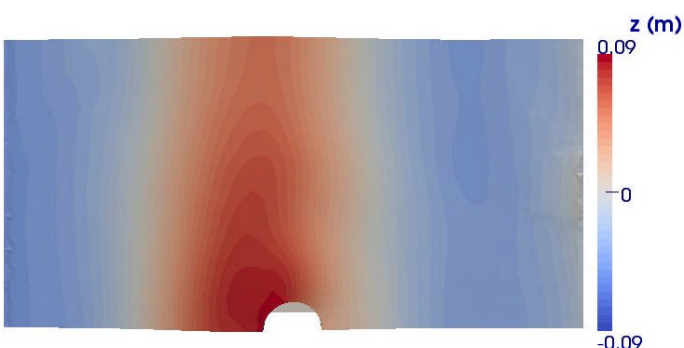
(a)  $t = 9.06$  s



(b)  $t = 9.19$  s

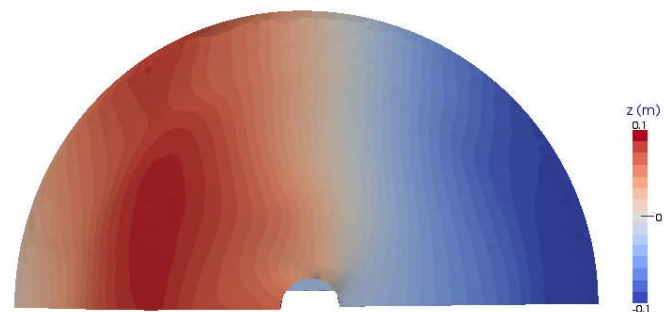


(c)  $t = 9.68$  s

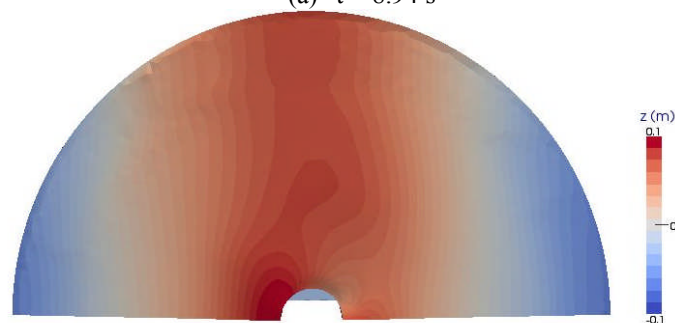


(d)  $t = 9.80$  s

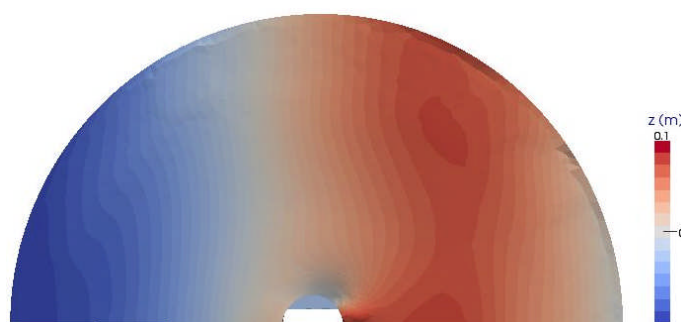
Fig. 8 Surface-Elevation Contour in Rectangular Numerical Wave Tank ( $h = 1.5$  m,  $a = 0.15$  m,  $T = 1.2$  s,  $\lambda/a = 15.9$ ,  $kA = 0.244$ ,  $H/a = 1.2$ )



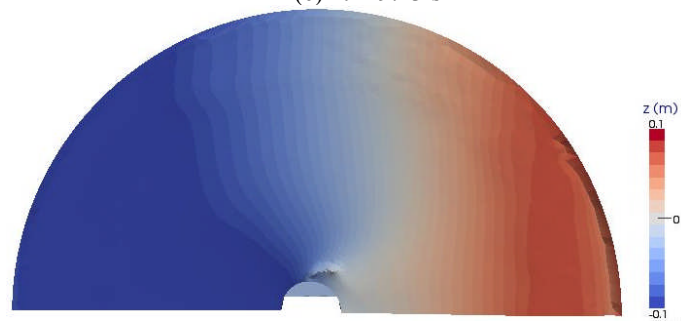
(a)  $t = 8.94$  s



(b)  $t = 9.19$  s



(c)  $t = 9.43$  s



(d)  $t = 9.68$  s

Fig. 9 Free-Surface Elevation Contour in Circular Numerical Wave Tank ( $h = 1.5$  m,  $a = 0.15$  m,  $T = 1.7$  s,  $\lambda/a = 30.4$ ,  $kA = 0.2$ )

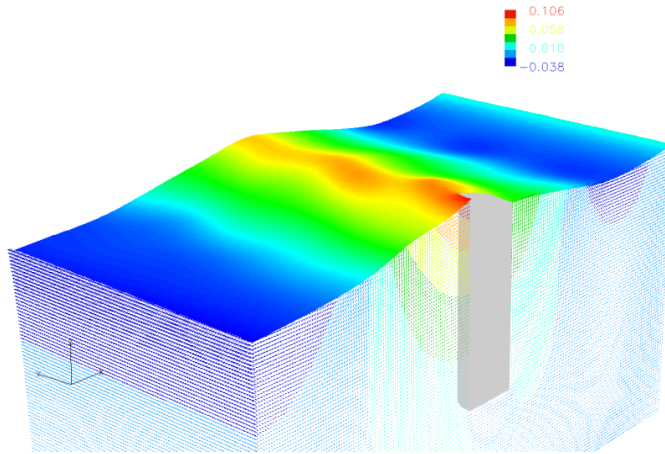


Fig. 10 Wave Elevation and Velocity Field in Rectangular Wave Tank ( $h = 1.5$  m,  $a = 0.15$  m,  $T = 1.2$  s,  $\lambda/a = 15.9$ ,  $kA = 0.244$ )

Fig. 9 shows the contour plots of free-surface elevation for the Case 2 with  $kA = 0.2$ . Wave crest line is obscure because the wave length is three times longer than domain radius. Local disturbances are mostly observed near the downstream-side of outer boundary. Wave run-up comparison with the theoretical and experimental results shows that the local disturbances are confined near the outer boundary and affect little on the near-field solution. In Fig. 10 contours of vertical component of ALE mesh displacement are shown on free surface. Also plotted are fluid velocity vector in the interior domain colored by vertical component of mesh displacement.

In Fig. 11, wave run-up,  $R$ , which is the wave elevation at  $x = -0.15$  m and  $y = 0$  m, are plotted with the input wave elevation at the same location. Significant amplification of wave elevation can be found. The wave run up reaches its stationary condition soon after one period.

Fig. 12 shows the calculated wave run-up for all wave steepness simulated. Comparisons are made with the theoretical values from WAMIT first- and second-order calculation, and model test data by [4]. Good agreements can be found between CFD result and model test data. For the highest wave steepness simulated,  $kA = 0.233$ , CFD result slightly over-predicts wave run up. The first-order theory under-predicts wave run up significantly. Because of long wave length, which is about 30 times of the cylinder radius, linear potential theory predicts negligibly small wave diffraction. The second-order theory improves the prediction but still under predicts. Nondimensionalized harmonic components of wave run up is also compared in Fig. 13. Fourier coefficients of wave run-up are obtained by the numerical integration at the last two periods of simulation. CFD results agrees well with the model test data except for the third-harmonic component for the lower wave steepness of  $kA = 0.16$ .

CFD simulation has been performed on a Linux Cluster with 43 Opteron-based compute nodes connected by Infiniband

switches. Computational time for Case 2 is about 12 s for each time step, which is 1/140 of one wave period.

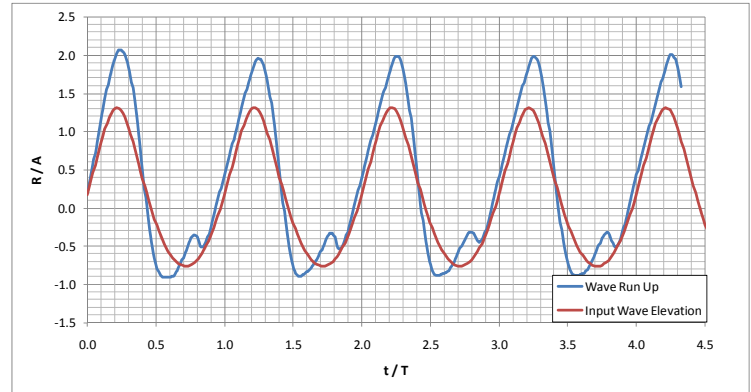


Fig. 11 Wave Run-up Compared with Input Wave Elevation ( $h = 1.5$  m,  $a = 0.15$  m,  $T = 1.7$  s,  $\lambda/a = 30.4$ ,  $kA = 0.233$ )

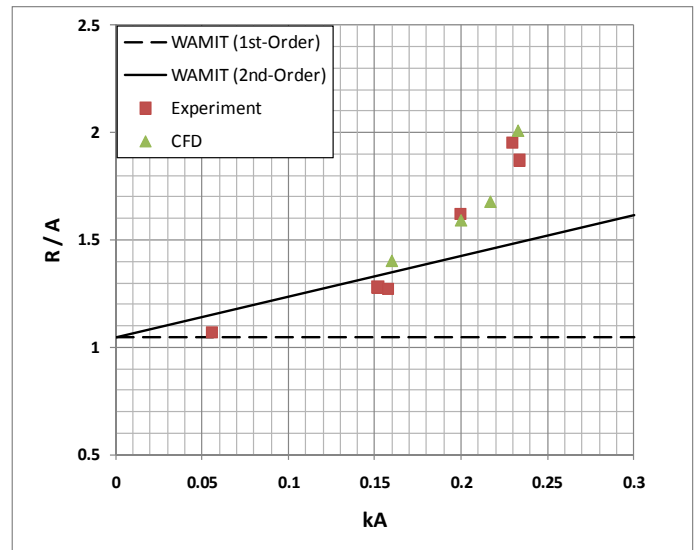
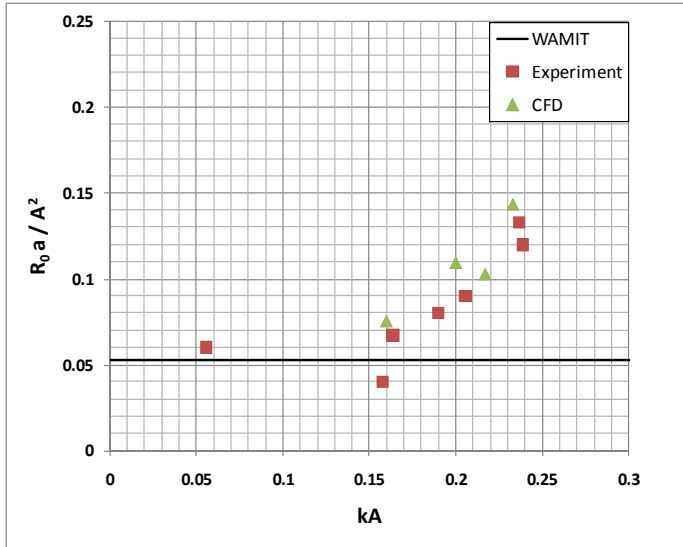
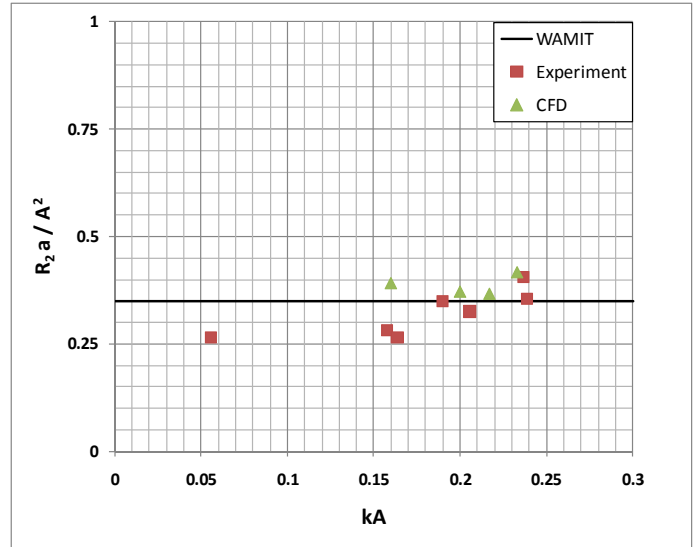


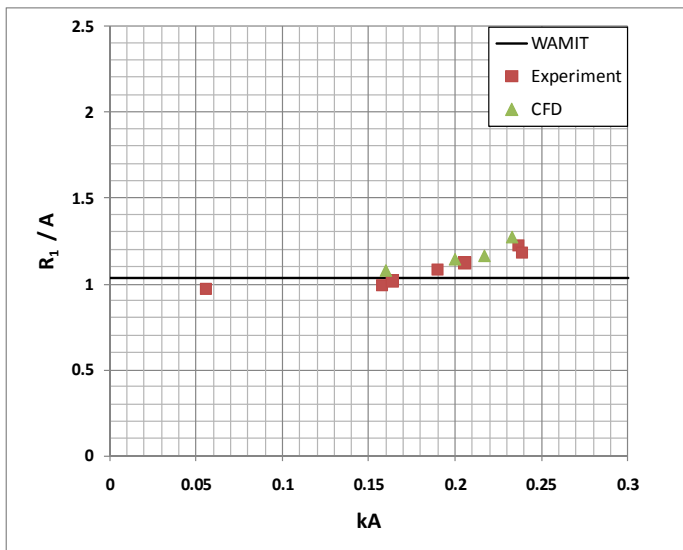
Fig. 12 Wave Run-up Compared with Theoretical and Experimental Results ( $h = 1.5$  m,  $a = 0.15$  m,  $T = 1.7$  s,  $\lambda/a = 30.4$ )



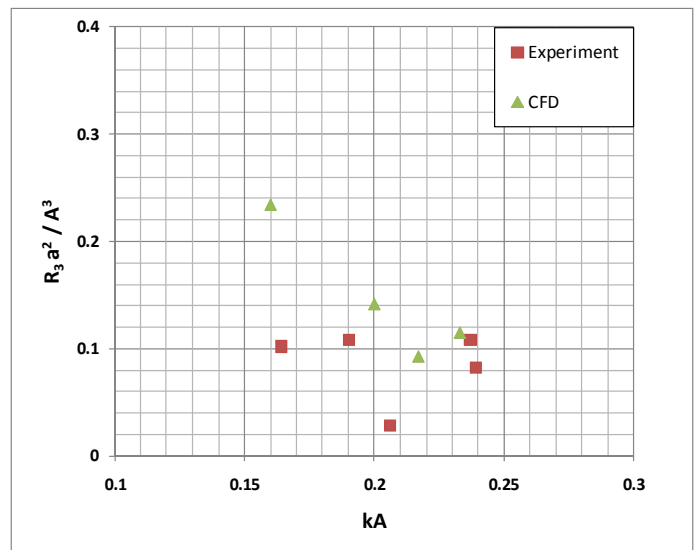
(a) Mean Value



(c) Second Harmonic



(b) First Harmonic



(c) Third Harmonic

Fig. 13 Harmonic Components of Wave Run-up Compared with Theoretical and Experimental Results ( $h = 1.5$  m,  $a = 0.15$  m,  $T = 1.7$  s,  $\lambda/a = 30.4$ )

## CONCLUSIONS

An efficient numerical wave tank model has been developed by matching far-field wave solution based on potential theory and the near-field CFD solution based on Navier-Stokes equation. The new model has been applied to a CFD code based on ALE Finite-Element method. The developed method is applied to a wave run-up simulation of a truncated vertical cylinder exposed to nonlinear regular waves with wave length much longer than cylinder diameter. Comparison with the theoretical and test data shows that the new method predicts wave run-up accurately

with small computational domain confined near the cylinder. In one of the simulation case, computational domain with radius only one third of the wave length provided wave run-up prediction accurate enough for the engineering purpose. The developed method will provide an efficient numerical wave tank to analyze air-gap problem of floating structures under the harsh environment with long wavelength and high steepness, with computational domain confined near the floater and modeling only a fraction of incoming wave length.

## ACKNOWLEDGMENTS

The authors would like to thank Technip for permitting publication of this paper.

## REFERENCES

- [1] Kim, J.W., Kyoung, J.H., Ertekin, R.C. and Bai, K.J. 2006 "Finite-Element Computation of Wave-Structure Interaction between Steep Stokes Waves and Vertical Cylinders," *J. Waterway, Port, Coastal, and Ocean Engineering*, Vol. 132, No. 5, pp. 337-347.
- [2] Kim, J.W., Kyoung, J.H., Bai, K.J. and Ertekin, R.C. 2004 "A Numerical Study of Nonlinear Diffraction Loads on Floating Bodies due to Extreme Transient Waves," 25<sup>th</sup> Symposium on Naval Hydrodynamics, St. John's, Newfoundland and Labrador, CANADA
- [3] Kriebel, D. L. 1992 Nonlinear Wave Interaction with a Vertical Circular Cylinder – Part II: Wave Run-Up, *Ocean Engng*, **19**(1), 75-99.
- [4] Morris-Thomas, M.T. and Thiagarajan, K.P. 2004, "The Run-Up on a Cylinder in Progressive Surface Gravity Waves: Harmonic Components," *Appl. Ocean Research*, Vol. 26, pp. 98-113.
- [5] Swan, C., Taylor, P. H. and van Langen, H. "Observation of wave-structure interaction for a multi-legged concrete platform" *Applied Ocean Research*, **19**, 1997, pp. 309-327.
- [6] Clauss G.F., Cshmittner, C.E. and Stuck R., 2005 "Numerical Wave Tank – Simulation of Extreme Waves for the Investigation of Structural Responses," *Proc. OMAE 2005*, Halkidiki, Greece.
- [7] Donea, J., "Arbitrary Lagrangian-Eulerian finite element methods", *Computational Methods for Transient Analysis*, Elsevier Science Publisher, pp. 474-516, 1983.
- [8] Bai, K.J. and Kim, J.W. 1995 "A Finite-Element Method for Free-Surface Flow Problems," *Theor. Appl. Mech.* Vol. 1, No. 1, pp. 1-27.
- [9] AcuSolve, General Purpose CFD Software Package, Release 1.7f, ACUSIM Software, Mountain View, CA, 2008.